Rock Mechanics and Rock Engineering (2021) 54:71–89
https://doi.org/10.1007/s00603-020-02265-2

ORIGINAL PAPER

A Limit Equilibrium Model of Tabular Mine Pillar Failure

J. A. L. Napier[1] · **D. F. Malan**[1]

Received: 28 April 2020 / Accepted: 29 September 2020 / Published online: 15 October 2020

Abstract

An improved understanding of pillar strength and pillar failure mechanisms is required to optimize tabular mine layout designs. The paper describes the application of a limit equilibrium model for pillar failure analysis. It is shown that the model is capable of reproducing a hardening or softening response for uniformly compressed strip or square pillars. The stress–strain behavior depends on three non-dimensional parameters Q, M and β. Q represents the ratio of the limit failed uniaxial strength to the intact material strength, M is the ratio of the failed limit strength envelope slope to the intact strength envelope slope and β is proportional to the pillar width to height ratio. The model is implemented in a displacement discontinuity solution scheme using unstructured triangular elements to allow irregular plan-view pillar shapes and mining step increments to be represented. The seam-parallel confining stress distribution in the fracture zone is determined using a fast marching solution algorithm. A case study of an experimental pillar extraction site in a platinum mine is presented to illustrate the capability of the model to simulate the evolution of pillar failure as pillar extraction proceeds. Good qualitative agreement to observed failure trends are obtained but the detailed calibration of the model parameters remains a challenge. Further work is required to enhance the representation of pillar edge spalling processes.

Keywords Pillar failure · Limit equilibrium model · Fast marching method · Tabular mine layout · Triangular elements

1 Introduction

A number of shallow coal or hard rock mines employ pillar mining systems as a strategy for roof failure control (Van der Merwe and Madden 2010; Ryder and Jager 2002). In certain platinum mine layouts, pillars are designed to "crush" in a stable manner as they become loaded in the panel back area (Du Plessis and Malan 2015). The correct sizing of pillars demands some knowledge of the pillar strength and the overall layout stress distribution. It is particularly important to understand the impact of the layout extraction pattern on the effective regional “stiffness” of the rock mass around each pillar and to assess the macroscopic response of the overburden region as mining progresses.

Two broad strategies may be followed to achieve a satisfactory pillar layout design. The traditional approach is to employ empirically determined pillar strength formulas to select the pillar dimensions (see, e.g., Lunder and Pakalnis 1997; Martin and Maybee 2000; Gonzalez-Nicieza et al. 2006; Watson et al. 2008; Esterhuizen et al. 2011). This approach can lead to conservative designs in which pillars are over-sized with a corresponding reduction in the overall mine life and profitability and are not directly useful in exploring evolutionary stress distribution trends as mining progresses. Large scale pillar collapses have also been observed in mines, where empirical pillar strength formulas could not account for the effect of weak partings on pillar strength (Malan and Napier 2011; Esterhuizen et al. 2019). The second strategy is to model relatively detailed layout configurations which include a precise representation of the local plan view of the layout geometry and to analyse multiple mining scenarios and extraction sequences to select optimal pillar sizes and barrier pillar spacing. The displacement discontinuity boundary element method provides a useful representation of laterally extensive tabular mine layouts and has been extensively employed in the design of coal, gold and platinum mining operations (Plewman el al. 1969; Deist el al. 1972; Crouch and Starfield 1983; Salamon 1964; Ryder and Napier 1985; Heasley 1998). The main drawback of this technique is the neglect of the detailed excavation stress distribution in the normal direction to the mining horizon near

---

✉ D. F. Malan
francois.malan@up.ac.za

[1] Department of Mining Engineering, University of Pretoria, Pretoria, South Africa

excavation edges. This difficulty can be addressed by devising simplified local models of the excavation edge failure region boundary conditions which are suitably coupled to the host displacement discontinuity solution mesh.

The present paper explores the use of a simple limit equilibrium model of the edge failure zone using an unstructured triangular element mesh to represent the generally irregular pillar and excavation shapes. The major computational requirement is to solve the seam-parallel confining stress distribution and to identify the location of the fracture zone edge. The so-called "fast marching" or "fast sweeping" technique developed by (see Osher and Sethian 1988; Sethian 1999) has been described by Napier (2016) and by Napier and Malan (2018) for the solution of longwall tabular excavations using square element grids. The present paper describes the extension of this approach to the solution of triangular element mesh tessellations with specific emphasis on the solution of pillar layout problems. Analytic models of the failure of a strip pillar and a square pillar are presented initially to illustrate the behavior of the limit model. These models are then compared to the predicted response of the average pillar stress that is calculated using the fast marching technique. The preliminary calibration of the model against observed stress and pillar deformation observations obtained from an underground field study is described in the final section.

2 Fast Marching Solution for the Seam-Parallel Confining Stress in an Unstructured Triangular Element Mesh

As mining progresses the edges of hard rock or coal mining excavations are generally fractured. If it is assumed that the fracture zone is in a state of mobile equilibrium and that the vertical extent of this fracture zone is bounded by stratified geological features such as parting planes or other layering, it is possible to construct a differential force balance for the average seam-parallel and seam-normal tractions that obeys a relationship of the form:

$$H\left|\nabla\sigma_s(P)\right| = 2\mu_I\sigma_n(P) \tag{1}$$

where H is the fracture zone height normal to the excavation horizon, $\nabla\sigma_s(P)$ is the gradient vector of the average seam-parallel confining stress σ_s at point P in the excavation plane and σ_n is the seam-normal compressive traction component at point P. μ_I is the friction coefficient at the upper and lower interface discontinuity contacts separating the fractured material from the outer region of intact rock. Equation (1) is a more general form of a class of limit equilibrium models that have been proposed previously to describe the failure of coal pillars utilizing the confined core concept suggested by Wilson (1972). This concept has been employed notably by (Barron (1984), Barron and Pen (1992)) to develop analytic descriptions of pillar stress profiles. A detailed critique of this approach discussing some of the important limitations has been presented by Salamon (1992). The form of the limit model given by Eq. (1) allows for general orientations of the seam-parallel confining stress gradient in the fracture zone (Napier (2016), Napier and Malan (2018)). The only constitutive parameter representing the interface behavior is the effective friction coefficient, μ_I. More elaborate interface conditions are not investigated here. The mechanical response implied by this model in defining the fracture zone extent and the overall response of simplified pillar shapes to uniform pillar compression is investigated in Sect. 3. Some illustrations of actual pillar damage and layout response are given in Sect. 6.

The seam-normal compressive traction component σ_n at point P is determined by a limit equilibrium strength relationship $\sigma_n = f(\sigma_s)$ which, in the present case, is assumed to be a simple linear function:

$$\sigma_n(P) = \sigma_c(P) + m(P)\sigma_s(P) \tag{2}$$

where $\sigma_c(P)$ and $m(P)$ are the local strength envelope intercept and slope parameters at point P. In the present analysis it is assumed as well that the ratio $\kappa = \sigma_c(P)/m(P)$ is constant at all points P. In this case, Eq. (1) can be expressed in the form

$$|\nabla U| = 2\mu_I m(P)/H \tag{3}$$

by introducing the transformed solution variable U given by

$$U = \ln\left[\kappa + \sigma_s\right] \tag{4}$$

The solution to the eikonal Eq. (3) can be obtained on an unstructured triangular element mesh using the so-called "fast marching" algorithm as described, for example, by Osher and Sethian (1988), Kimmel and Sethian (1998) and Sethian (1999). The most direct approach is to obtain the solution at the covering displacement discontinuity triangular element vertices. However, the displacement discontinuity solution of mine layout problems is usually determined at one or more collocation points that are located within each element. In the simplest case, a single collocation point is located at the center of each element and the discontinuity value is assumed to be constant within each element. To accommodate this case, an alternative triangular fast marching solution grid is constructed which includes both the discontinuity element center points and the element vertices. The structure of this triangular mesh is illustrated in Fig. 1 for a portion of an irregular shaped pillar. The basic discontinuity element edges are plotted as solid lines. The edges of the fast marching solution mesh are shown as broken lines

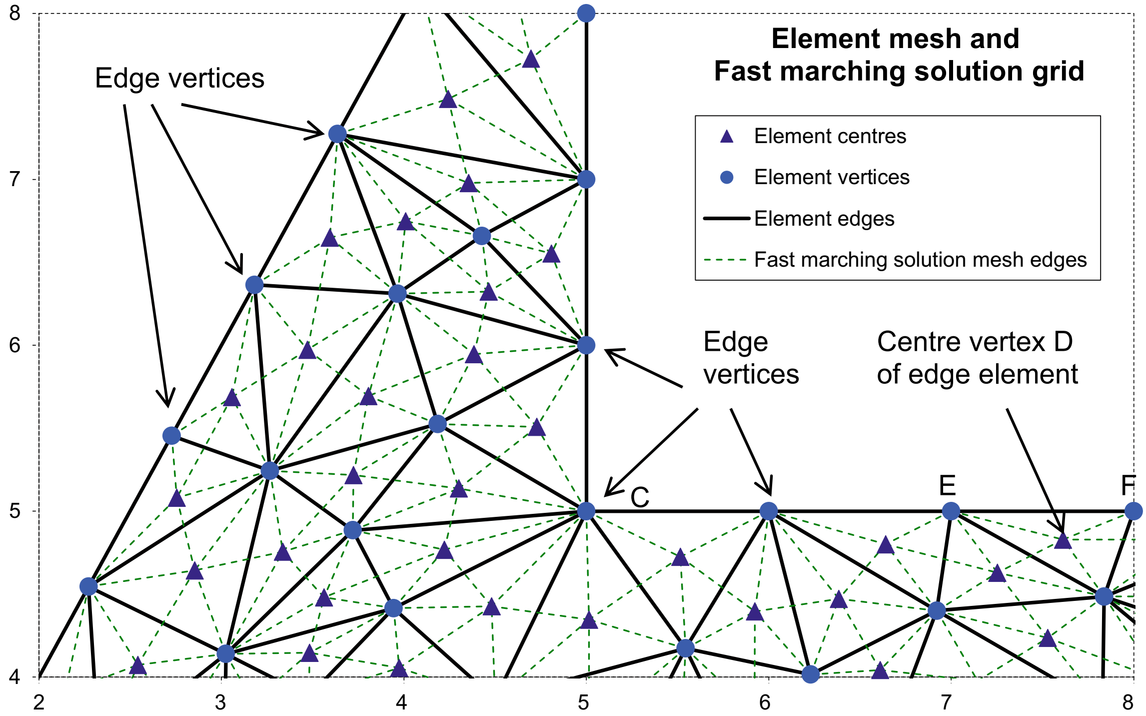

Fig. 1 Fast marching solution grid covering the parent displacement discontinuity triangular element mesh centers and vertices. Some typical edge vertices are shown as indicated

and are seen to have vertices which correspond to both the parent element mesh centers (triangular shaped markers) and to the parent mesh vertices (circular shaped markers).

The transformed seam-parallel confining stress variable U can be found by applying the fast marching solution algorithm with the boundary condition of $\sigma_s = 0$ at the edge vertices of the solution grid mesh (see Fig. 1). The local gradient direction at an edge vertex is assumed to be perpendicular to the edge tangent or to bisect the angle formed by successive edge segments in the case of a corner vertex such as C in Fig. 1. A fixed boundary condition value is also assigned at the centers of each edge element (for example, point D in Fig. 1). In these cases it is assumed that the confining stress gradient direction is perpendicular to the adjacent element edge at the excavation boundary. For example, the boundary value for σ_s at point D is determined by integrating Eq. (3) in the direction perpendicular to edge EF in Fig. 1 assuming that $\sigma_s = 0$ on EF. If the perpendicular distance from EF to D is equal to d it can be shown from Eq. (3) that

$$\sigma_s(d) = (\sigma_c/m)[\exp(2\mu_I md/H) - 1] \tag{5}$$

A general layout analysis will require the solution of the displacement discontinuity values for a series of excavation mining steps. The limiting seam-parallel and seam-normal stress values arising at each element collocation point P_C are evaluated by solving Eq. (3) at the start of each solution stage using the fast marching solution technique. The fast marching algorithm constructs this solution in a series of steps by examining all designated "trial" vertices that are adjacent to "known" assigned solution values (Kimmel and Sethian 1998; Sethian 1999). A typical trial vertex is depicted at vertex C in Fig. 2. The trial vertex is surrounded by one or more triangles such as ABC in Fig. 2. If the values of the solution variable U in Eq. (3) are known at the points A and B then the solution variable at point C can be evaluated to match the specified right hand side value defined in Eq. (3). This process is repeated for all sectors surrounding each trial vertex. The overall minimum trial value U^* is then designated to have a "known" status. This procedure is repeated until all solution vertices reach a "known" status. The main advantage of the fast marching procedure (Sethian 1999) is that the computational cost is proportional to $N \log N$, where N is the number of vertices in the solution mesh. In the present case, this does not add an appreciable computational cost to the overall iterative solution time for a given mine layout.

Once the limiting seam-parallel and seam-normal stress values have been determined it is possible to establish the displacement discontinuity solution values at each collocation point using a suitable iterative strategy. The displacement discontinuity solution for extensive tabular layouts can be found efficiently using an iterative hierarchical influence

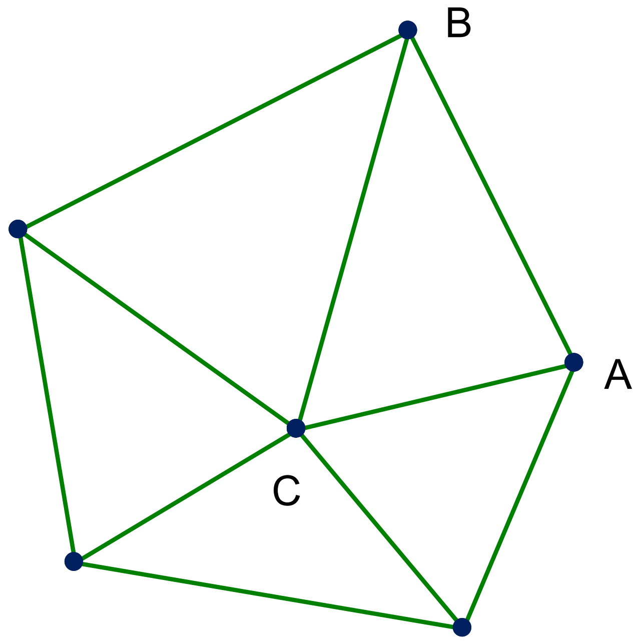

Fig. 2 Schematic layout of triangular solution mesh surrounding a trial vertex located at point C. Line AB represents a typical neighbour sector edge

"lumping" scheme as described, for example, by Napier and Malan (2007). In the present case each collocation point is examined in turn within an iteration cycle and the seam-normal stress value is evaluated assuming that no failure has occurred at the point. This value is then compared to the assumed intact strength value σ_n^* at the point P_C given by

$$\sigma_n^* = \sigma_c^i + m_i \sigma_s(P_C) \tag{6}$$

where σ_c^i and m_i are specified intact strength intercept and slope parameters and $\sigma_s(P_C)$ is the limit equilibrium solution value for the seam-parallel confining stress. The intact status at point P_C is maintained if no failure is deemed to occur. If failure does occur the displacement discontinuity solution value $\Delta u_n(P_C)$ is selected to yield a seam-normal stress value corresponding to the required limit value $\sigma_n(P_C)$. The iteration cycles are repeated until a defined error tolerance in the solution values is satisfied.

As an example, consider an irregular pillar shape as shown in Fig. 3. The pillar is tessellated using triangular displacement discontinuity elements and is embedded in a small rectangular mined region extending from local Cartesian coordinates (– 4, – 3) to (14, 12). The specific

Fig. 3 Irregular pillar shape example illustrating the edge failure zone and the locally assigned gradient contour directions at each element collocation point

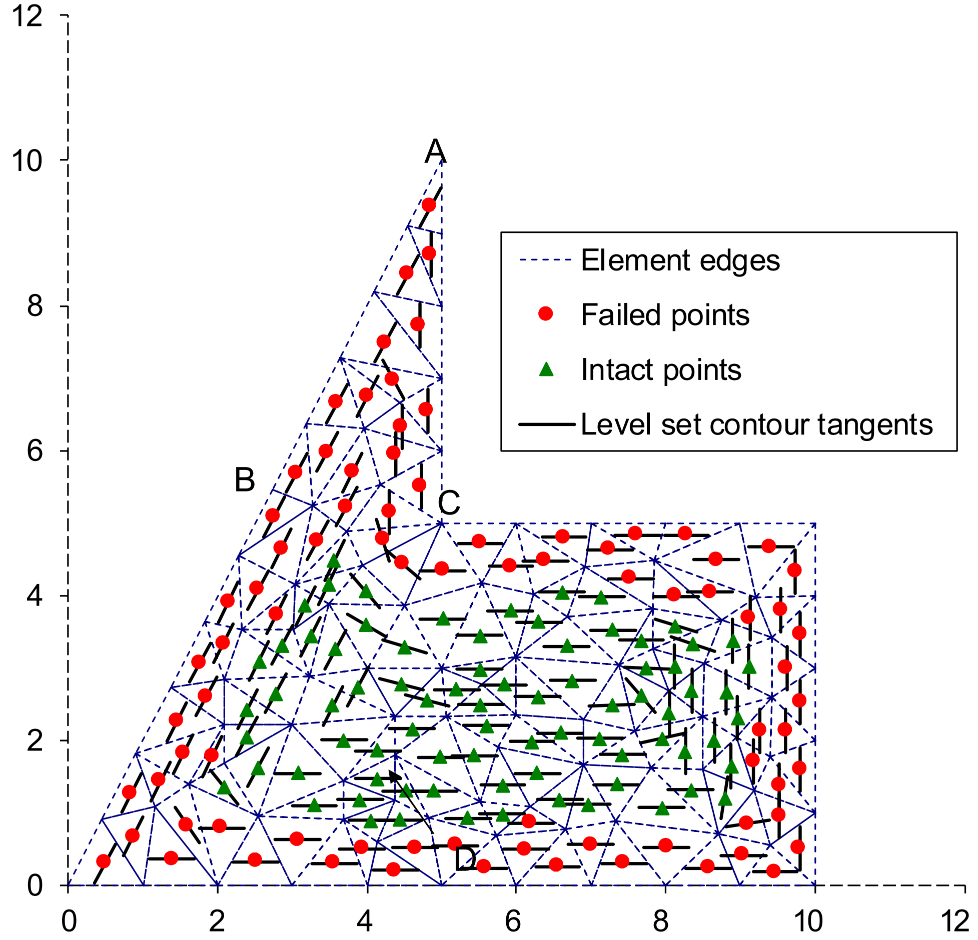

parameters that are used in the analysis are summarized in Table 1. The resulting failed region and the level set gradient contour tangent directions at each element collocation point are shown in Fig. 3. Complete failure occurs in the triangular region ABC and the extent of the intact core region is evident (see points depicted by triangular shaped markers). It is noted as well that the local edge gradient direction at points A and D is resolved according to the nearest excavation edge segment which yield a resolution that is limited by the assigned tessellation mesh size.

Table 1 Parameters used to illustrate structured and unstructured mesh solutions of the reef-parallel stress distribution in a pillar region

Parameter	Value
Intact strength intercept, σ_c^i	73.0 MPa
Intact strength slope, m_i	7.0
Residual strength intercept, σ_c	46.0 MPa
Residual strength slope, m	4.6
Effective seam height, H	3.0 m
Intact rock Young's modulus, E	70,000.0 MPa
Intact rock Poisson's ratio, ν	0.2
Fracture zone interface friction angle,φ_I	20°
Field stress normal to excavation plane	60.0 MPa

3 Analytic Model of Pillar Failure

3.1 Strip Pillar Model

The stress–strain response of the limit equilibrium model description of platinum mine crush pillars or coal mine panel and barrier pillars is controlled by a number of critical parameters. It is important to gain some insight into the role of these parameters in determining the average stress–strain response of a pillar with a given pillar shape (specifically, the contrast between strip pillars, square pillars and irregular shaped pillars) and the behavior of the model as the pillar width to height ratio is varied. In addition, it is necessary to assess whether the simple limit model structure that has been proposed should be amended in cases, where the pillar width, W, becomes small compared to the height, H (e.g., $W/H < 2$).

Consider, initially, the case of a long strip pillar having a width, $W = 2a$, with a central intact elastic core region of width $W_0 = 2a_0$ as depicted in Fig. 4 and assume that a uniform compression is applied across the pillar. Let a local coordinate x designate the distance from the center of the pillar. The stress distribution in the fractured edge zone is then given by the one-dimensional version of Eq. (3) which can be seen to be expressed as

$$\sigma_n(x) = \sigma_c + m\sigma_s(x) = \sigma_c \exp(2\mu_I m(a-x)/H), \; a_0 \le x \le a \tag{7}$$

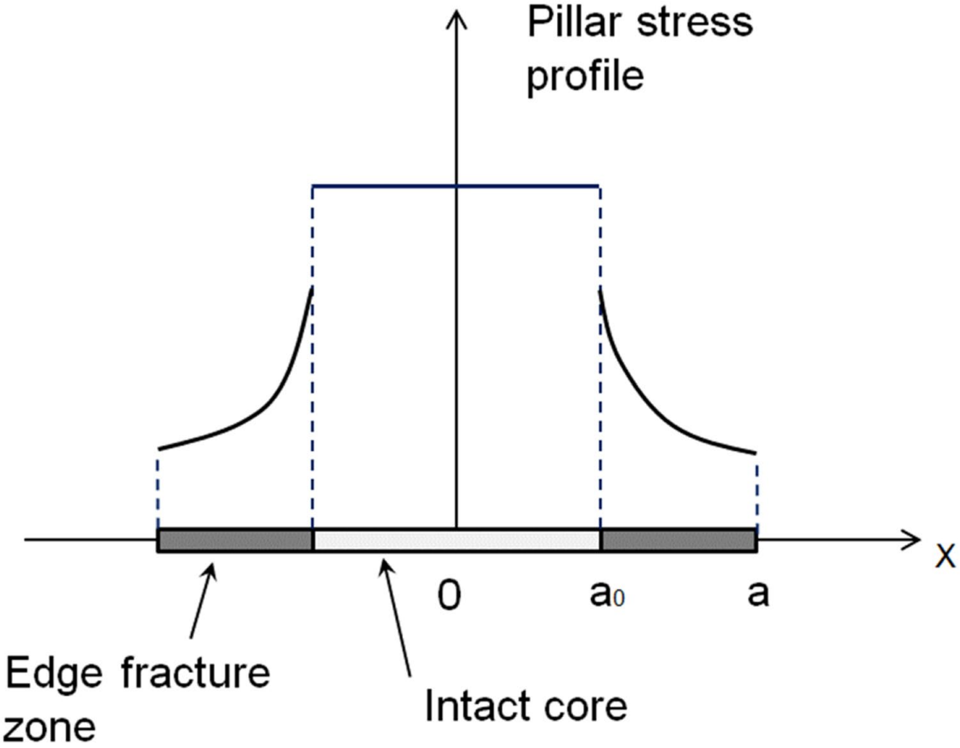

Fig. 4 Conceptual stress profile across a uniformly compressed strip pillar having an intact elastic core region

where $\sigma_s(x)$ and $\sigma_n(x)$ are, respectively, the average seam-parallel and the seam-normal stress components at position x. σ_c and m are the residual limit equilibrium strength envelope parameters and μ_I is the friction coefficient at the interface between the fractured material and the bounding intact rock. H is the effective height of the pillar.

Assume that the average stress $\overline{\sigma}_n^E$ in the central core of the pillar is given by a linear elastic relationship of the form:

$$\overline{\sigma}_n^E = E_S \varepsilon \tag{8}$$

where E_S is the effective pillar material modulus and ε is the average pillar strain. The maximum strain that can be sustained by the pillar will depend on the extent of the edge fracture zone and on the intact rock strength properties. Assume that the intact core strength envelope is given by $\sigma_c^i + m_i \sigma_s(a_0)$, where σ_c^i and m_i are the intact rock uniaxial strength and slope parameters, respectively, and $\sigma_s(a_0)$ is the seam-parallel confining stress at the edge of the central intact region. The pillar strain can then be inferred to be given by

$$E_S \varepsilon = \sigma_c^i + m_i \sigma_s(a_0) \tag{9}$$

The seam-parallel stress $\sigma_s(a_0)$ can be deduced from Eq. (7) to be

$$\sigma_s(a_0) = (\sigma_c/m)\,[\exp(2\mu_I m(a - a_0)/H] \tag{10}$$

Let $\overline{\sigma}_n^A$ be the average stress in the fractured region adjacent to the intact core. By integrating Eq. (7) it can be shown that

$$(a - a_0)\overline{\sigma}_n^A = \frac{\sigma_c H}{2\mu_I m}\left\{\exp[2\mu_I m(a - a_0)/H] - 1\right\} \tag{11}$$

The average stress $\overline{\sigma}_n$ across the whole pillar is then given by the weighted expression

$$a\overline{\sigma}_n = a_0 \overline{\sigma}_n^E + (a - a_0)\overline{\sigma}_n^A \tag{12}$$

Combining Eqs. (7) to (11), it is possible to use Eq. (12) to infer a relationship between the average pillar stress and strain. To simplify this expression, it is useful to define the dimensionless width to height ratio parameter β to be

$$\beta = 2\mu_I m a/H = \mu_I m W/H \tag{13}$$

and to define the non-dimensional strength parameter ratios

$$M = m/m_i \text{ and } Q = \sigma_c/\sigma_c^i \tag{14}$$

It is envisaged in this analysis that $M \le 1$ and that $Q \le 1$. In addition, define the scaled edge fracture zone length ϕ to be

$$\phi = 1 - (a_0/a) \tag{15}$$

The parameter ϕ may be viewed alternatively as a form of "damage" variable which ranges from $\phi = 0$ (intact pillar) to $\phi = 1$ when the pillar core is completely fractured. If the strain across the pillar is increased from zero, the pillar will remain intact until the pillar stress reaches the postulated intact uniaxial strength σ_c^i. At this point, let the average strain be ε_0, where

$$E_S \varepsilon_0 = \sigma_c^i \tag{16}$$

The scaled pillar strain χ and the scaled average pillar stress A are now defined to be

$$\chi = \varepsilon/\varepsilon_0 \tag{17}$$

$$\text{and } A = \overline{\sigma}_n/\sigma_c^i \tag{18}$$

Substituting these dimensionless parameters into Eqs. (9) and (10), yields the expression

$$\chi = 1 + (Q/M)[e^{\beta\phi} - 1] \tag{19}$$

The scaled average pillar stress A can be inferred from Eq. (12) to be

$$A = (1 - \phi)\chi + Q[e^{\beta\phi} - 1]/\beta \tag{20}$$

Finally, solving Eq. (19) for φ and substituting this result into Eq. (20) yields the scaled strip pillar average stress–strain relationship in the form

$$A = \chi - \frac{\chi}{\beta}\ln\left[1 + (M/Q)(\chi - 1)\right] + (M/\beta)(\chi - 1); \chi \ge 1 \tag{21}$$

It is important to note that when $0 \le \chi \le 1$, $A = \chi$ and the pillar stress–strain relationship is elastic. The fracture zone extent, reflected by the parameter ϕ, increases steadily when $\chi > 1$ and the pillar is completely fractured when $\phi = 1$. Defining the scaled strain value $\chi = \chi^*$ and scaled average pillar stress $A = A^*$ when $\phi = 1$, it can be seen from Eqs. (19) and (20) that

$$\chi^* = 1 + (Q/M)[e^{\beta} - 1] \tag{22}$$

$$\text{and } A^* = Q[e^{\beta} - 1]/\beta \tag{23}$$

The slope of the scaled average strip pillar stress relation (21) is given by

$$A'(\chi) = 1 + \frac{M}{\beta} - \frac{\chi}{\beta[\chi + (Q/M) - 1]} - \frac{1}{\beta}\ln\left[1 + (M/Q)(\chi - 1)\right] \tag{24}$$

The average pillar load will decrease at the onset of pillar failure, when $\chi = 1$, if $A'(1) < 0$. This occurs if the scaled width to height parameter β is smaller than a critical value given by

$$\beta < (M/Q)(1 - Q) \tag{25}$$

3.2 Square Pillar Model

Consider a square pillar with an overall width $W = 2a$ and with a central core region of width $W_0 = 2a_0$, as depicted in Fig. 5. For constant limit strength parameters σ_c and m the seam-normal stress at a point in the pillar is determined by the closest distance from the point to the edge of the pillar. The pillar behavior is assumed to be symmetric in the four triangular regions depicted by the dashed lines in Fig. 5. The normal stress at a distance $x - a$ from the nearest edge is given by Eq. (7) and the average stress $\overline{\sigma}_n^A$ in the fractured region is determined from

$$\left(a^2 - a_0^2\right)\overline{\sigma}_n^A = 2\int_{a_0}^{a} x\sigma_n(x)dx \tag{26}$$

The scaled average pillar stress is expressed by a weighted combination of the average stress in the core region and the surrounding fractured region according to the relationship

$$A = \frac{\overline{\sigma}_n}{\sigma_c^i} = \left(\frac{a_0}{a}\right)^2 \frac{\sigma_n^E}{\sigma_c^i} + \left[1 - \left(\frac{a_0}{a}\right)^2\right] \frac{\sigma_n^A}{\sigma_c^i} \tag{27}$$

Employing the same dimensionless quantities defined for the strip pillar analysis and evaluating Eq. (26), it can be shown that Eq. (27) can be expressed as

$$A = (1 - \phi)^2\chi + \left(2Q/\beta^2\right)\left\{[1 + (1 - \phi)\beta]e^{\beta\phi} - \beta - 1\right\} \tag{28}$$

where the scaled fracture zone length parameter ϕ is given by

$$\phi = (1/\beta)\ln[1 + (M/Q)(\chi - 1)] \tag{29}$$

The scaled strain value $\chi = \chi^*$ that arises when the intact core is completely fractured occurs when $\phi = 1$. In this case χ^* is again given by Eq. (22) and, from Eq. (28),

$$A^* = \left(2Q/\beta^2\right)\left\{e^{\beta} - \beta - 1\right\} \tag{30}$$

The condition for immediate softening of the pillar once failure is initiated at $\chi = 1$ is given by

$$\beta < (2M/Q)(1 - Q) \tag{31}$$

It is also of interest to note that the slope of the scaled average square pillar stress given by Eq. (22) can be expressed as a function of the edge damage fraction ϕ in the form

$$A'(\chi) = \frac{(1-\phi)M}{\beta Q}\left\{Q\left[2 + \frac{(1-\phi)\beta}{M}\right] - 2e^{-\beta\phi} - \frac{2Q}{M}\left(1 - e^{-\beta\phi}\right)\right\} \tag{32}$$

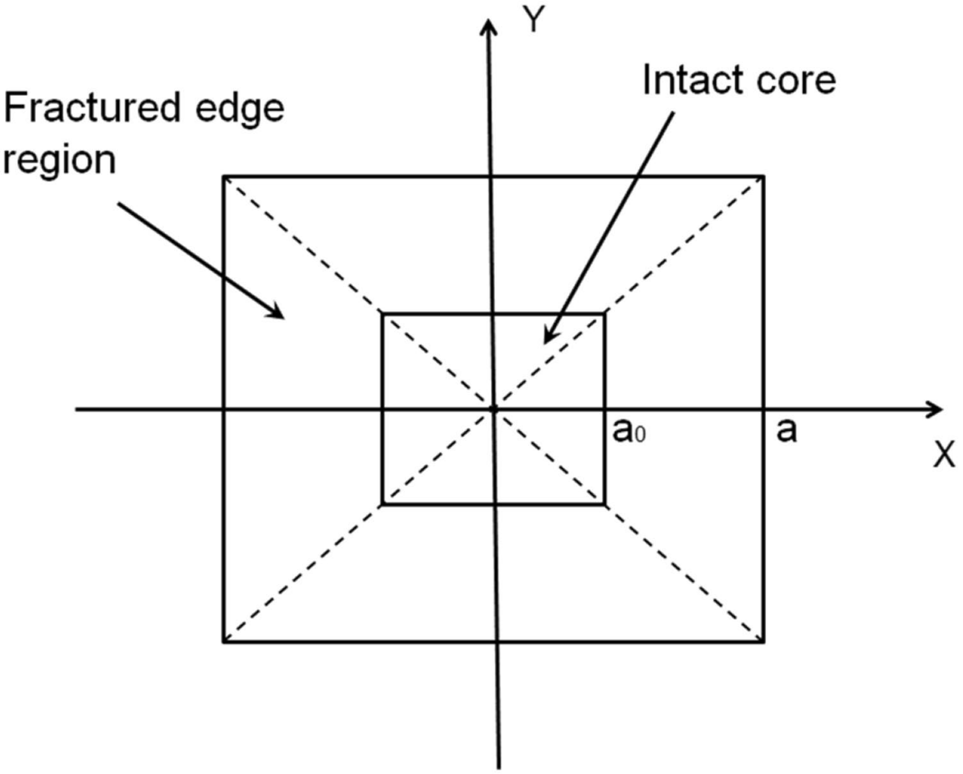

Fig. 5 Square pillar plan view with the intact core region area equal to $4a_0^2$ and the overall pillar area equal to $4a^2$

where ϕ depends implicitly on χ through Eq. (29). It is observed from Eq. (32) that when $\phi = 1$, $\chi = \chi^*$ and $A'(\chi^*) = 0$.

4 Critical Parameter Values Controlling Square Pillar Stress–Strain Behavior

The condition provided by Eq. (31) for immediate softening (load reduction) at the onset of square pillar failure can be expressed alternatively as

$$Q < 1/[1 + (\beta/2M)] \tag{33}$$

where Q is the scaled uniaxial strength ratio parameter (see Eq. (14)). This condition can be contrasted to the constraint that the final average pillar stress A^* is greater than the average pillar stress at the onset of failure. It can be seen from Eq. (32) that $A^* > 1$ provided

$$Q > \frac{\beta^2}{2(e^\beta - \beta - 1)} \tag{34}$$

Equations (33) and (34) provide limiting bounds on the range of the parameter Q, expressed as functions of M and β, which determine either the initial softening or hardening behavior of the average pillar stress and the residual softened or hardened state when the central core is completely fractured. These relations are depicted graphically in Fig. 6. Equation (34) is plotted as the thick line marked as the "residual softening boundary". Equation (33) is plotted as a series of curves in Fig. 6 with the parameter M set to the values 0.2, 0.4, 0.6, 0.8 and 1.0, respectively. Figure 6, therefore, enables the general pillar response to be predicted for a given choice of values of Q, M and β. To illustrate this, consider the particular case, where $M = 0.4$ and where Q and β correspond to the marked points A, B, C, D and E in Fig. 7. The specific parameter values and the expected pillar behavior is summarized in Table 2.

The scaled average pillar stress values for the four points A, B, C and D are plotted as a function of the scaled strain values in Fig. 8 and confirm the predicted behavior that is inferred from Fig. 7 and summarized in Table 2. Similar stress–strain response curves can be plotted for a strip pillar with the same scaled parameter values that are used for points A, B, C and D. It is observed that the average pillar stress values for cases B, C and D are significantly larger than for the square pillar. Strip pillar softening occurs also for case A at the onset of pillar failure. It should be noted that the initial softening condition given by Eq. (25) differs from the condition for a square pillar given by Eq. (31).

It is important to note as well that in all cases, where the initial stress–strain response slope is positive (i.e., when $A'(1) > 0$), the peak pillar stress will always exceed the residual stress when the pillar core is completely failed (i.e., there will always exist a local maximum value $\hat{A}$ of A in the range $1 < \chi < \chi^*$ such that $\hat{A} > 1$).

It is of interest to note as well the special case defined by point E in Fig. 7 and summarized in the last line of Table 2. In this case, it is predicted that the residual strength of the square pillar will be greater than the initial failure strength

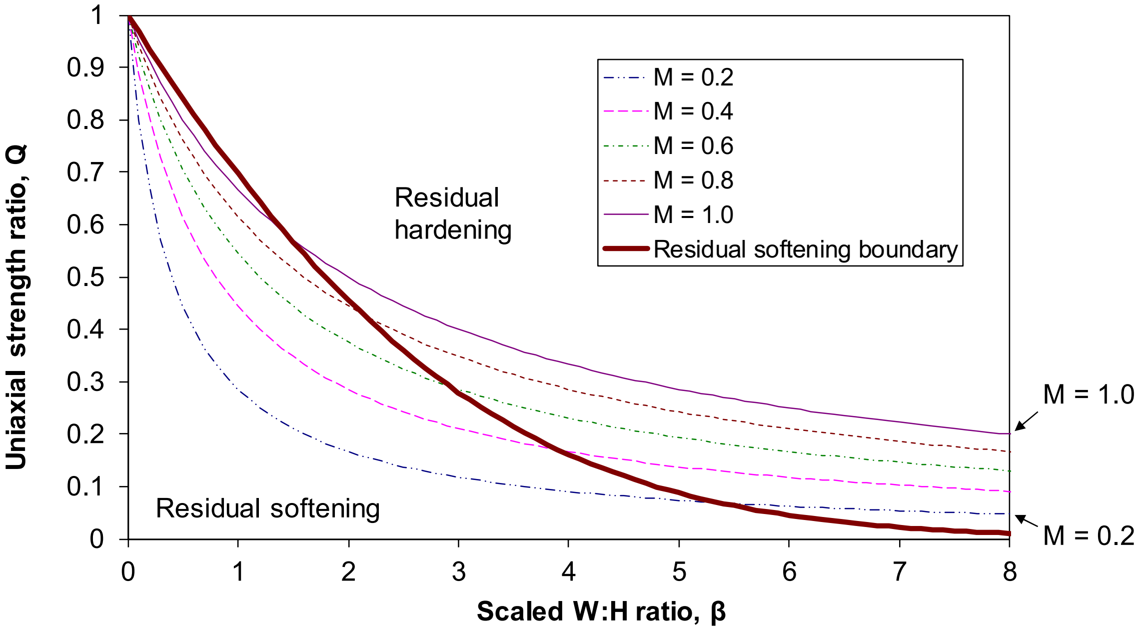

Fig. 6 Critical region boundaries for square pillar residual softening or hardening

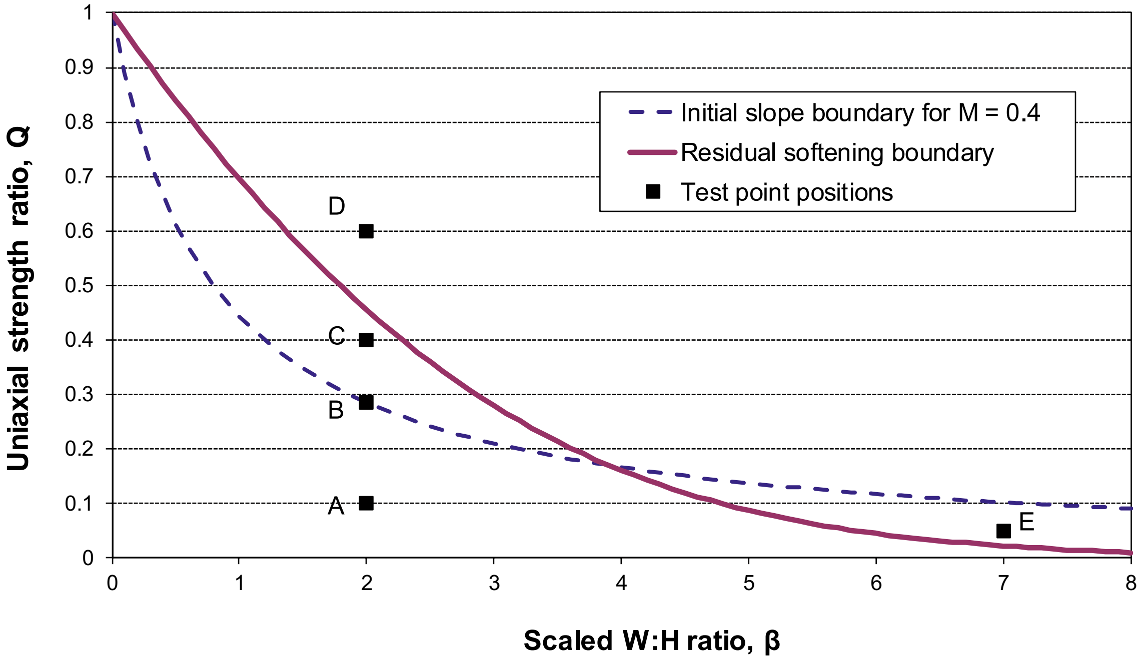

Fig. 7 Parameter space test points for illustrative square pillar stress–strain curves (Slope ratio parameter, $M = 0.4$)

Table 2 Parameter values and expected pillar behavior corresponding to points A, B, C, D and E in Fig. 7

Point	Q	β	M	Initial slope, $A'(1)$	Final stress, A^*
A	0.20	2.0	0.4	Negative	Softened (< 1)
B	0.28571	2.0	0.4	Zero	Softened (< 1)
C	0.40	2.0	0.4	Positive	Hardened (> 1)
D	0.60	2.0	0.4	Positive	Hardened (> 1)
E	0.05	7.0	0.4	Negative	Hardened (> 1)

but that there is a small initial load decrease in the average pillar stress value at the onset of failure.

5 Comparison of the Fast Marching Solution to the Analytic Model for A Square Pillar

In this section the analytic square pillar solution is compared to the crush zone extent that is found when using the fast marching scheme for two particular cases. In the first case, the numerical solution was applied to a square pillar with a width of 9.0 m and with the height parameter set to 2.0 m. The pillar was tessellated using 580 triangular elements and successive uniform compression strain steps were applied to the pillar. The applied compression is used to infer the intact stress magnitude from the assumed elastic modulus of the pillar. This stress can be compared to the failure condition implied by Eq. (6) at each collocation point P_C. If the compressive displacement discontinuity component is designated by $\overline{D}_n$ the element is assumed to fail if.

$$k_S\overline{D}_n \geq \sigma_c^i + m_i\sigma_s(P_C) \tag{35}$$

where the seam-normal elastic compressive stiffness k_S is given by.

$$k_S = E_S/H \tag{36}$$

The seam-normal stress value of the failed point is assigned the limit value $\sigma_n(P_C)$ if failure occurs at point P_C. The average pillar stress values corresponding to a series of applied pillar compression values are compared to the analytic square pillar solution in Fig. 9. The assumed parameter values are included in the figure legend. The numerically computed average pillar stress values can be seen to be in good agreement with the analytic solution.

A second test was performed to evaluate the average pillar response when post peak pillar softening occurs. In this case, it was postulated that the peak pillar stress was equal to σ_c^i and that the initial post peak softening slope has a specified value $-k_S^{PP}$. Utilizing Eq. (32) for the scaled initial slope $A'(1)$ of the average pillar stress–strain relationship and the definitions of the dimensionless parameters M ,Q and β it can be shown that the specification of the value of k_S^{PP} can be accommodated by imposing the following constraint on the pillar parameter values;

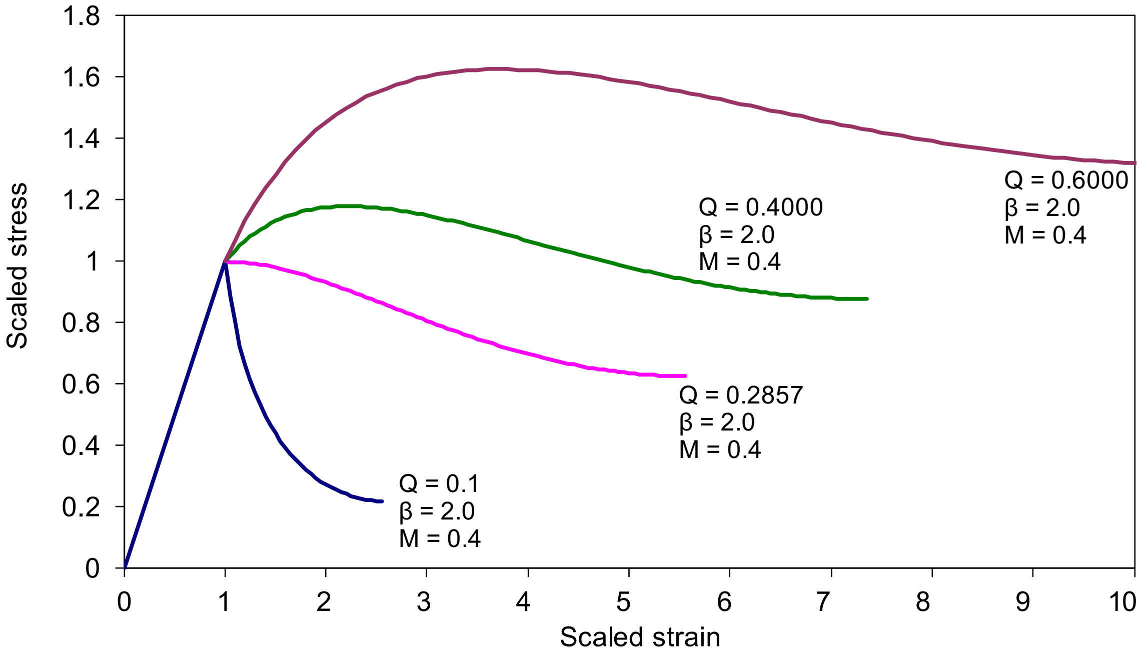

Fig. 8 Square pillar illustrative stress–strain curves at test points **a**, **b**, **c** and **d** marked in Fig. 4

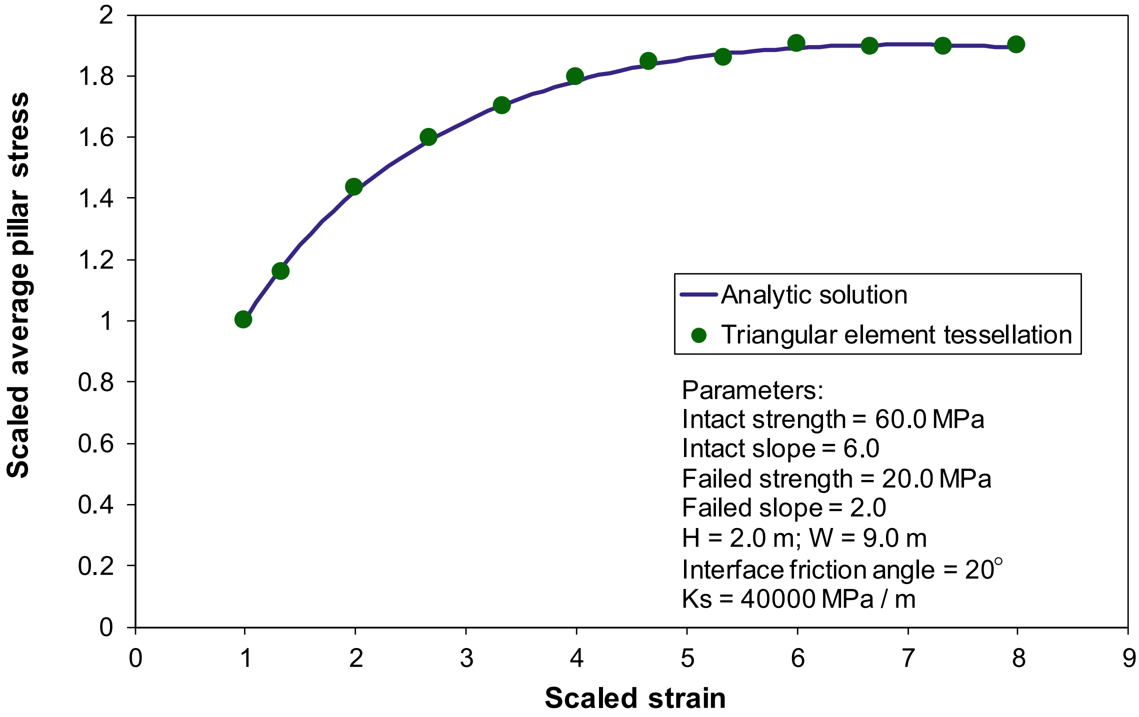

Fig. 9 Square pillar—hardening response

$$W/H - \frac{2[(\sigma_c^i/\sigma_c) - 1]}{\mu_I m_i[1 + (k_S^{PP}/k_S)]} = 0 \tag{37}$$

For example, choosing appropriate parameters in Eq. (37) allows a rough calibration of the pillar response to be made based on available field observations of the post peak pillar compression slope (see, for example, Wagner 1974). For example, selecting $k_S = k_S^{PP} = 2000$ MPa/m, $\sigma_c^i = 12.0$ MPa, $\sigma_c = 2.8$ MPa, $m_i = 6$ and $\mu_I = \tan(20°) \approx 0.36397$ requires that $W/H \approx 3/2$ for Eq. (37) to be satisfied. Figure 10 shows the simulated average stress response values for the case, where $W = 3.0$ m and $H = 2.0$ m compared to the analytic solution given by Eq. (28). The pillar was again tessellated using 580 triangular displacement discontinuity elements. Figure 10 shows good agreement between the numerically computed values and the analytic solution.

6 Field Study of Pillar Extraction

This section illustrates the application of the limit equilibrium model to a large-scale bord and pillar layout problem. An experimental pillar mining section was established in a platinum mine in the Eastern Bushveld Complex of South Africa. The mine is located near the town of Lydenburg and it exploits the tabular UG2 chromitite seam. The experimental section at the mine was established by mine personnel in an attempt to determine pillar strength more accurately. The pillar sizes at the mine were originally designed using the empirical Hedley and Grant power-law strength formula (Hedley and Grant 1972). This approach is currently considered to be too conservative for most of the shallow South African platinum mines. Ryder and Jager (2002) comment that this empirical formulation was adopted in the platinum mines as no data on local pillar behavior was available to derive strength formulae.

The experiment consisted of instrumenting a central pillar in an old mining area and progressively mining the pillars surrounding this pillar until failure of the central pillar occurred. Figure 11 illustrates the layout in this area. The designed pillar sizes were 9 m × 7 m and the bords were 8 m wide. This gives a theoretical extraction ratio of 75.3%. Small element sizes (average size ≈ 0.45 m^2) were used to minimize the effect of mesh size on the behavior of the limit equilibrium element simulations (Malan and Napier 2018). The total number of displacement discontinuity elements used to represent the area shown in Fig. 11 was 36 317. The actual extraction ratio could be calculated from the mesh as 76.6%. This illustrates good pillar cutting discipline as it is often difficult to maintain the designed pillar sizes in hard rock mines. The extraction

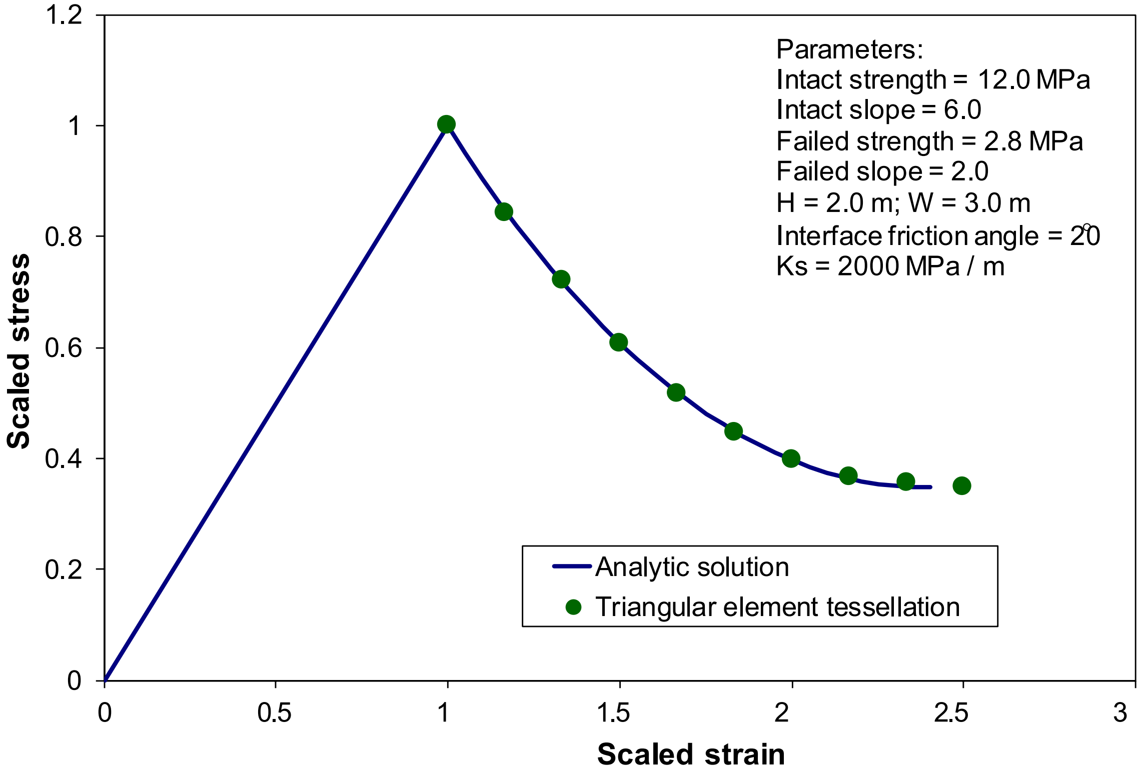

Fig. 10 Square pillar—softening response using selected values for the pillar stiffness and the post peak pillar softening slope

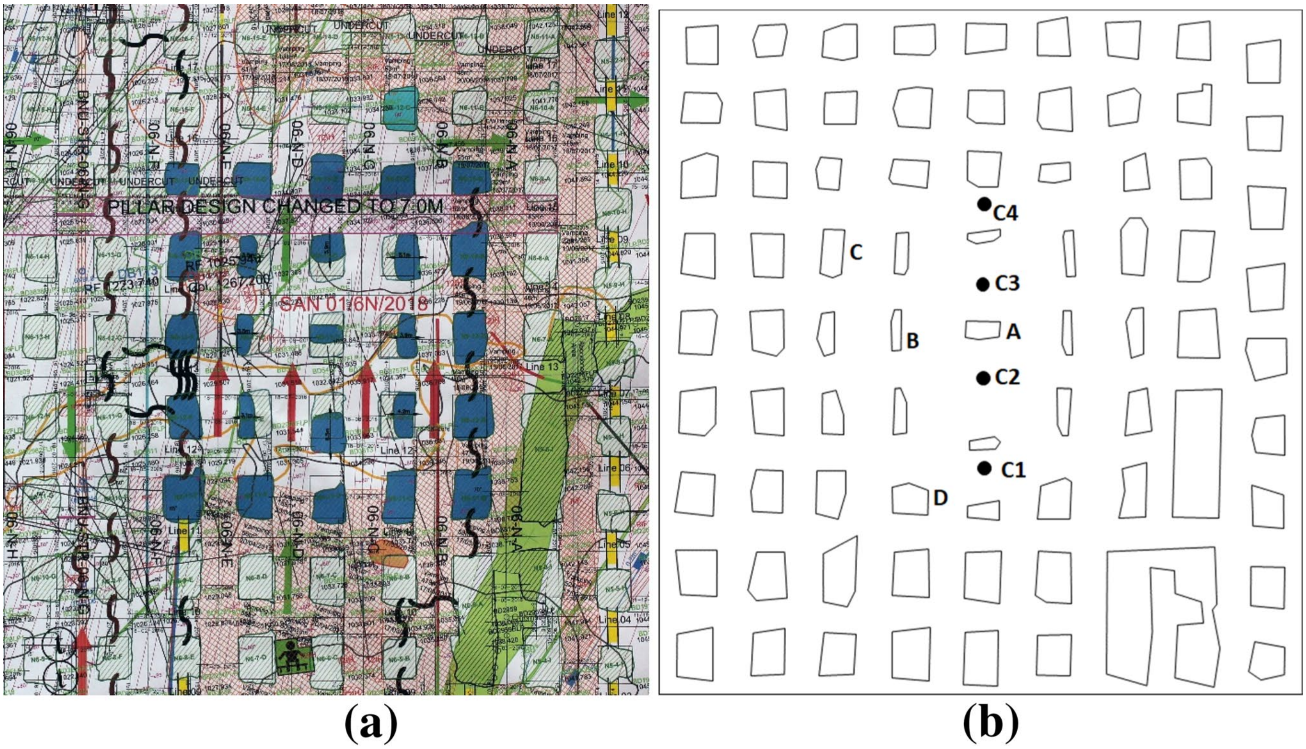

Fig. 11 **a** Layout of the experimental pillar mining area of a shallow bord and platinum mine. This diagram represents the size of the area simulated with dimensions of 136 m × 145 m. The pillars highlighted in blue, where gradually reduced in size to increase the load acting on the central pillar. **b** The final geometry of the central pillars when the experiment was stopped. The instrumented pillar is indicated as pillar A

ratio, depth (275 m) and estimated average overburden density (3000 kg/m^3) gives an average pillar stress of 36 MPa using tributary area theory calculations.

For computational efficiency, only the 25 pillars of interest in the center of the excavation were allowed to fail, while the outer pillars were simulated as “rigid” pillars that were not allowed to deform. In terms of the mining sequence,

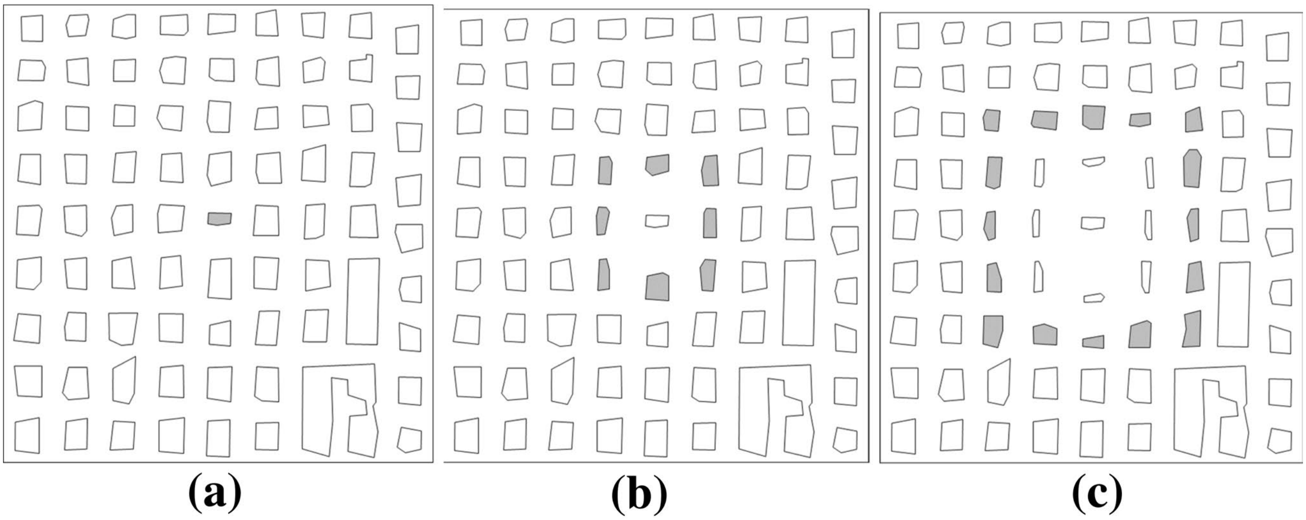

Fig. 12 Sequence of mining of the pillars: **a** reduction in size of pillar A to approximately 6.7 m × 3.6 m, **b** mining of the first ring of pillars, **c** mining of the second ring of pillars. This diagram illustrates the final geometry

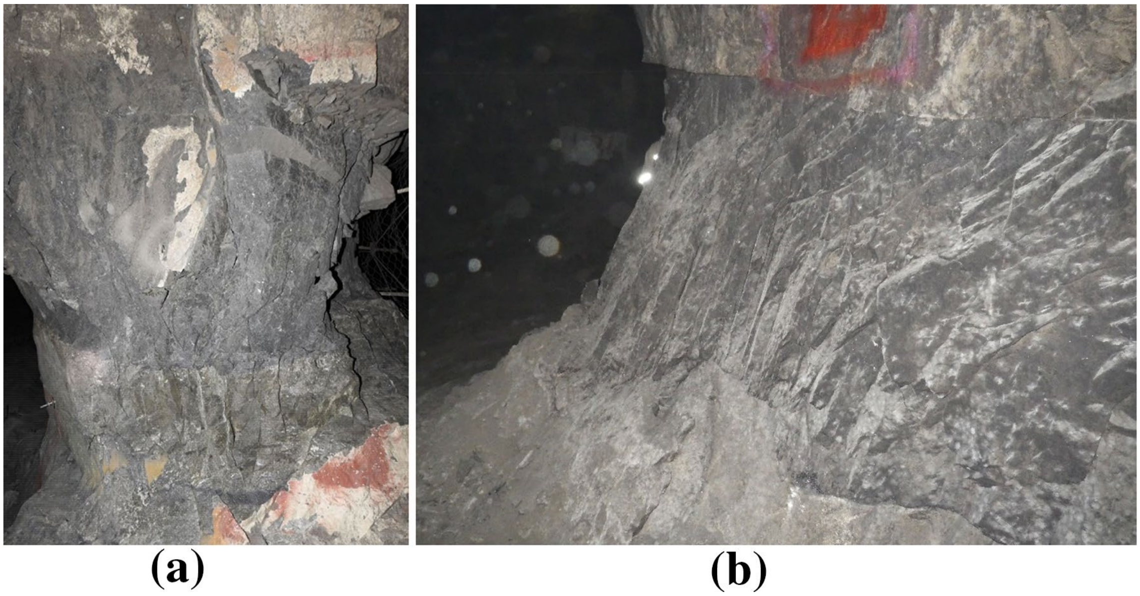

Fig. 13 Photographs illustrating the complex composition of the pillar material. **a** The darker rock is the chromitite and the lighter material is pyroxenite. **b** Some of pillars have a weak contact between the chromitite and pyroxenite, resulting in a failure mechanism reminiscent of the simplified limit equilibrium model

the central pillar was first reduced in size and then the adjacent two rings of pillars were gradually mined following the sequence shown in Fig. 12. The mining proceeded slowly and the experiment lasted from January 2018 to December 2019.

The depth of the excavation was 275 m and as the dip of the reef was small. Garza-Cruz et al (2019) have discussed the effect of shear stresses on pillar stability, but this is not considered in the present case study for the approximately horizontal seam. The average density of the rock was assumed to be 3000 kg/m^3 and the mining height was approximately 2.5 m. The calibration of the limit equilibrium parameters listed in Table 1 is difficult for actual pillar mining examples. The calibration given below was based on a number of trial and error simulations that are compared to the actual underground observations to guide the process. A parameter sensitivity study was conducted after a set of parameters was obtained which gave results that appeared to match the observations. It should be emphasized that the purpose of this modelling was to investigate the potential of the limit equilibrium failure model for the simulation of large scale, irregular shaped pillar failure problems and not to obtain precise calibration of all the parameters. The observations that were used to guide the calibration process were as follows.

The uniaxial compressive strength of the chromitite reef, as tested in the laboratory, varies from 137 to 197 MPa. The actual pillar edges are not homogenous and a pyroxenite waste band is present in the UG2 reef in this area (see Fig. 13). Weak partings are also present, and therefore, the large scale in situ uniaxial strength of the rock will be substantially lower than the laboratory strength. In situ tests on large rock specimens (Bieniawski and Van Heerden 1975) are not available in the present case. Laboratory shear tests on parting planes gave friction angles ranging from 32° to 35º.

It was observed that the pillars appeared to be stable before the mining of the pillars commenced and almost no fracturing or scaling was present at the edges of the pillars. As the outer pillars were reduced in size, the fracturing on these pillars increased and, at the final step, the smallest pillars were completely fractured (for example, pillar B illustrated in Fig. 14a).

Surprisingly, the instrumented central pillar (pillar A in Fig. 11b) showed only limited scaling as the stress gradually increased and by the end of the experiment this pillar was still mostly intact (Fig. 14b). The final width of this pillar was less than 4 m and the nominal mining height was 2.5 m. A decision was taken by the mine to terminate the experiment at this stage owing to the safety risk of the large spans and the adjacent failing pillars. The reason for the unexpectedly good final condition of pillar A is not clear.

A number of simulations were conducted to investigate the effect of the various parameters on the simulated pillar response. A list of these parameters is given in Table 3. It was assumed that Young's modulus was 70 000 MPa and Poisson's ratio was 0.2 for the intact rock. Using a mining depth of 275 m and an assumed vertical stress gradient of 0.03 MPa/m the virgin stress normal to the excavation plane was 8.25 MPa. The dip of the reef was assumed to be

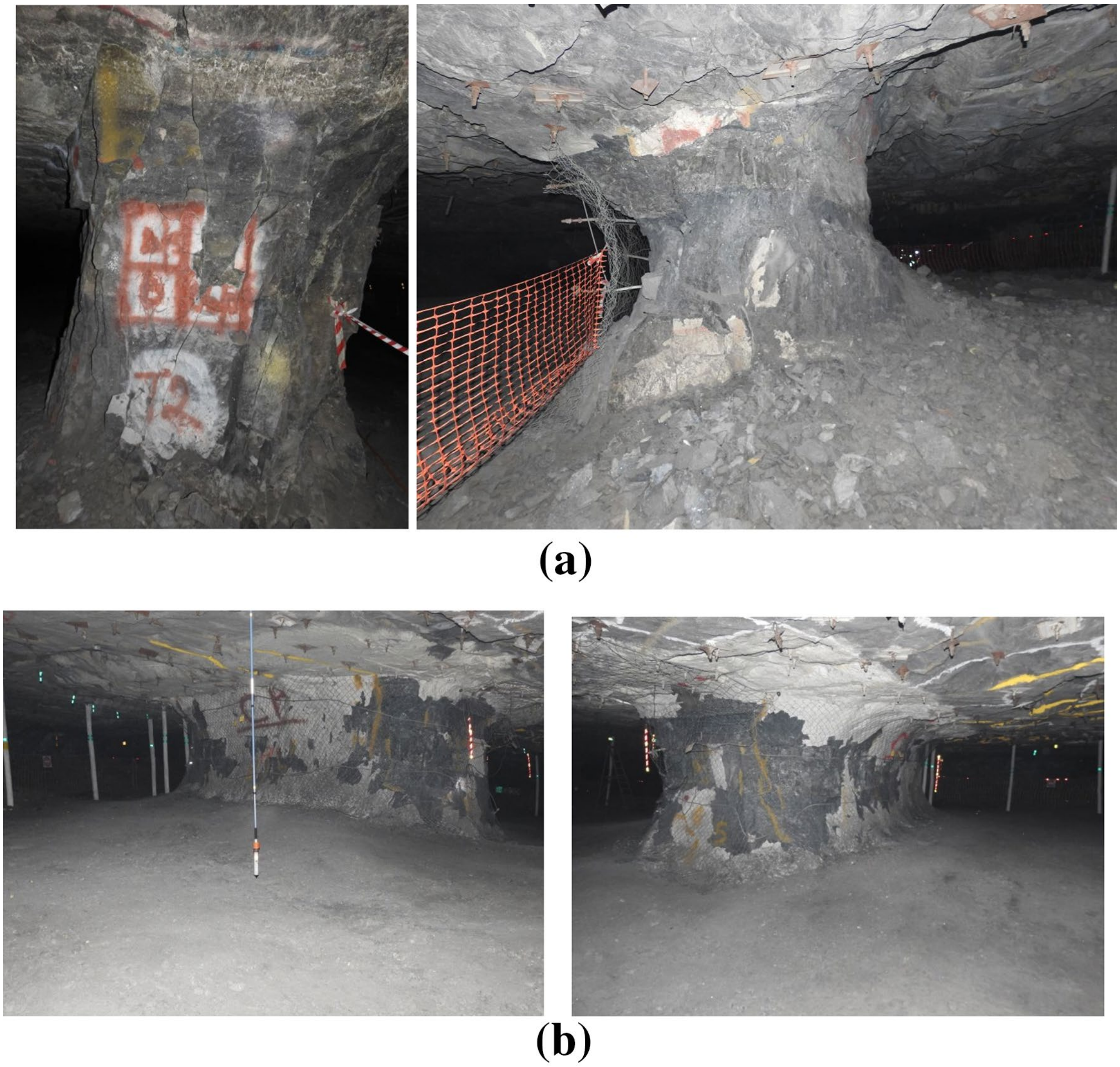

Fig. 14 **a** Typical failure of the small pillars (e.g., pillar B in Fig. 11b) surrounding the central pillar. The core of these pillars were fractured. **b** The instrumented pillar A photographed at the time when the experiment was terminated. The pillar was painted white as a visual indication of scaling of the sidewalls. Note the closure instrument in the foreground in the photograph on the left

0º. In Table 3, the parameters M, Q and β were calculated using Eqs. (13) and (14). The expected final stress condition shown in the table is for a failed square pillar and was determined using Eq. (33). Note that most of the calibration runs predict immediate softening (load reduction) at the onset of pillar failure. Calibration run 14, with high strength values, was included as a benchmark to calculate the pillar stresses if no failure occurs.

Table 4 illustrates some of the results from the simulations. This shows the failure behavior of pillars A, B, C and D (see Fig. 11b) for the parameters listed in Table 3. The approximate final dimensions of these pillars are A (6.7 m × 3.6 m), B (8.9 m × 1.7 m), C (9.6 m × 4.6 m) and D (7.6 m × 5.4 m). Pillar A is the central instrumented pillar and Pillar B is a slender crush pillar in the first ring of mined pillars. The average pillar stress (APS) (see Napier and Malan 2011) for each pillar is given in the table.

From the results in Table 4, pillar B (see Fig. 11b.) crushes completely for most of the calibration runs as observed. This is to be expected owing to the small width of this pillar (1.7 m). The final APS for pillar B is substantially reduced compared to the case, where the pillars remain intact (calibration run 14). It is of interest to note that for the pillars with a width close to 5 m or exceeding 5 m (pillars C and D), almost no reduction in APS occurs, even for substantial fracturing of the pillar edges (calibration run 11). Calibration runs 2 and 3 appear to match the underground observations best with pillar B completely crushed, only moderate failure for pillar A and almost no damage for the larger pillars such as C and D. These specific calibration

Table 3 Calibration runs to investigate the effect of the parameters on the simulated pillar behavior

Calibration run	Intact strength (MPa)	Intact slope	Residual strength (MPa)	Residual slope	Interface friction angle	Stiffness (MPa/m)	Seam height (m)	M	Q	β_1 W = 5 m	β_2 W = 2.5 m	Expected final stress (β_1)	Expected final stress (β_2)
1	40	7	4	7	30	28000	2.5	1.00	0.10	4.62	2.36	Softened	Softened
2	60	7	4	7	30	28000	2.5	1.00	0.07	4.62	2.36	Softened	Softened
3	70	7	4	7	30	28000	2.5	1.00	0.06	4.62	2.36	Softened	Softened
4	80	7	4	7	30	28000	2.5	1.00	0.05	4.62	2.36	Softened	Softened
5	60	7	3	7	30	28000	2.5	1.00	0.05	3.46	1.77	Softened	Softened
6	60	7	7.5	7	30	28000	2.5	1.00	0.13	8.66	4.42	Softened	Softened
7	60	7	10	7	30	28000	2.5	1.00	0.17	11.55	5.89	Hardened	Softened
8	60	5.8	4	5.8	30	28000	2.5	1.00	0.07	4.62	2.36	Softened	Softened
9	60	4.6	4	4.6	30	28000	2.5	1.00	0.07	4.62	2.36	Softened	Softened
10	60	7	4	4.6	30	28000	2.5	0.66	0.07	4.62	2.36	Softened	Softened
11	60	7	4	3	30	28000	2.5	0.43	0.07	4.62	2.36	Softened	Softened
12	60	7	4	7	25	28000	2.5	1.00	0.07	3.73	1.90	Softened	Softened
13	60	7	4	7	35	28000	2.5	1.00	0.07	5.60	2.86	Softened	Softened
14	200	7	200	7	50	28000	2.5	1.00	1.00	476.70	243.12	Hardened	Hardened

Table 4 Simulated pillar behavior for some of the pillars of interest

Calibration run	Pillar A failure	Pillar A APS (MPa)	Pillar B failure	Pillar B APS (MPa)	Pillar C failure	Pillar C APS (MPa)	Pillar D failure	Pillar D APS (MPa)	Closure C2 (mm)
1	58%	47.0	100%	21.6	37%	35.6	30%	35.4	10.0
2	51%	47.4	100%	21.6	2%	41.9	2%	40.8	9.6
3	42%	48.9	100%	21.6	0%	41.4	0%	40.2	9.2
4	16%	55.9	32%	59.4	0%	40.0	0%	38.8	8.4
5	58%	44.3	100%	16.2	11%	41.0	5%	40.3	9.9
6	34%	52.8	66%	49.3	0%	40.8	0%	39.7	8.8
7	25%	55.6	59%	53.7	0%	40.4	0%	39.4	8.6
8	59%	44.0	100%	15.7	11%	40.4	5%	40.5	10.0
9	73%	38.8	100%	11.5	18%	39.9	14%	39.3	10.6
10	62%	41.9	100%	11.5	11%	40.8	5%	40.9	10.2
11	97%	20.6	100%	8.0	31%	37.7	19%	38.9	11.3
12	60%	43.6	100%	15.1	11%	40.6	5%	40.6	10.0
13	41%	50.3	85%	35.8	1%	41.2	1%	40.0	9.1
14	0%	61.9	0%	72.5	0%	39.8	0%	38.7	8.2

The percentage failure for each pillar was calculated as the number of failed elements divided by the total number of elements

Fig. 15 The simulated failure in the pillars after the last mining step (calibration run 2). The dots indicate the failed elements

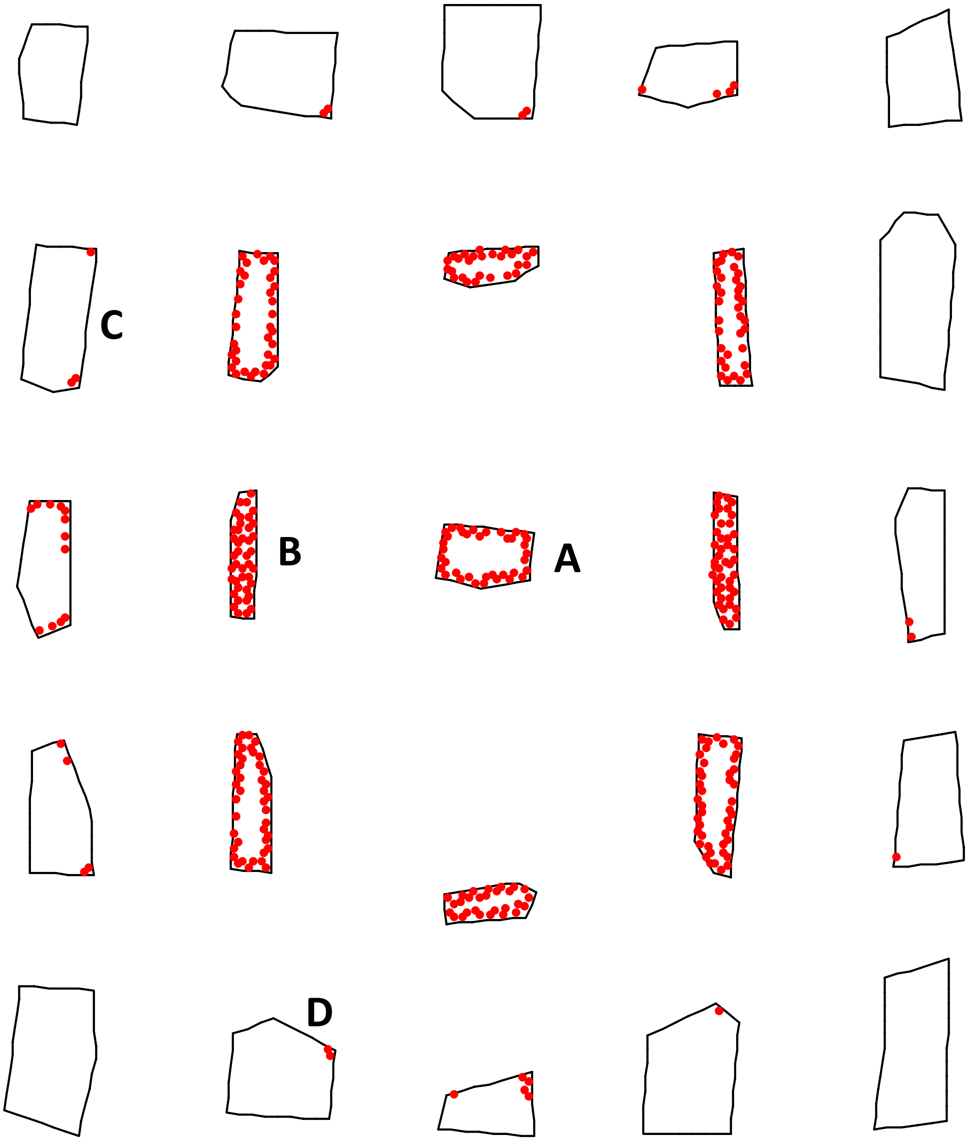

runs assumes a reasonable estimate for the in situ uniaxial strength of the pillar material of 60–70 MPa.

The failure of the pillars in the model for calibration run 2 is shown in Fig. 15. Note that the smallest pillars are completely fractured and pillar A still has an intact core. The model nevertheless seems to indicate a larger extent of fracturing in this central pillar compared to that observed underground (Fig. 14).

The measured and simulated increase in the closure at a number of points (see Fig. 11b) is shown in Fig. 16. The simulated closure is slightly less than the measured closure and displays a similar trend to the observed closure values. The observed and simulated increase in closure was the greatest for the two closure stations C2 and C3 that are the closest to the instrumented pillar (see Fig. 11b).

The simulated increase in average pillar stress for pillar A is shown in Fig. 17. This increase is the greatest for the case (calibration run 14), where no pillar failure occurred but is significantly lower for calibration run 2, where pillar failure occurs (see also Fig. 15). Stress measurements were conducted by the mine in the hangingwall above pillar A and a calculated peak average pillar stress of approximately 160 MPa was reported to the authors. There is a large discrepancy between this measured value and the simulated values presented in Fig. 17. The suggested pillar strength of 160 MPa exceeds the typical laboratory strength value of UG2 chromitite (137 MPa to 197 MPa) and is also counter-intuitive for a pillar with a width to height ratio of less than 1.6. Further work is required to confirm the hangingwall stress levels in these platinum mines.

Based on these preliminary results, it appears that the limit equilibrium model can provide a good qualitative

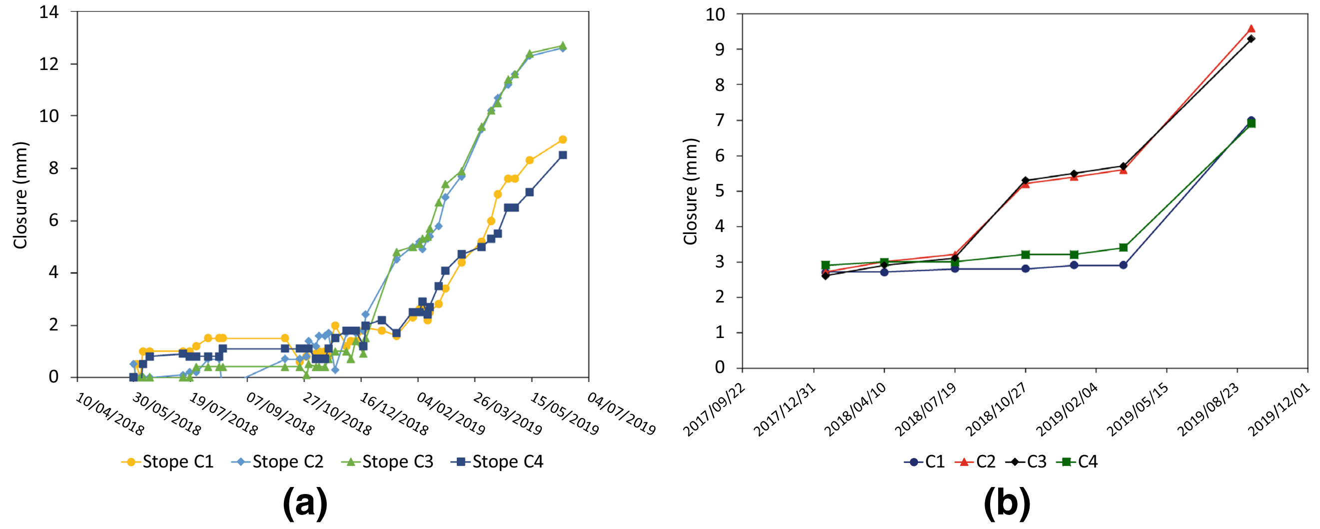

Fig. 16 Measured **a** and simulated **b** increase in closure at the four measurement positions (see Fig. 11b)

Fig. 17 Measured and simulated increase of the average pillar stress in the central pillar

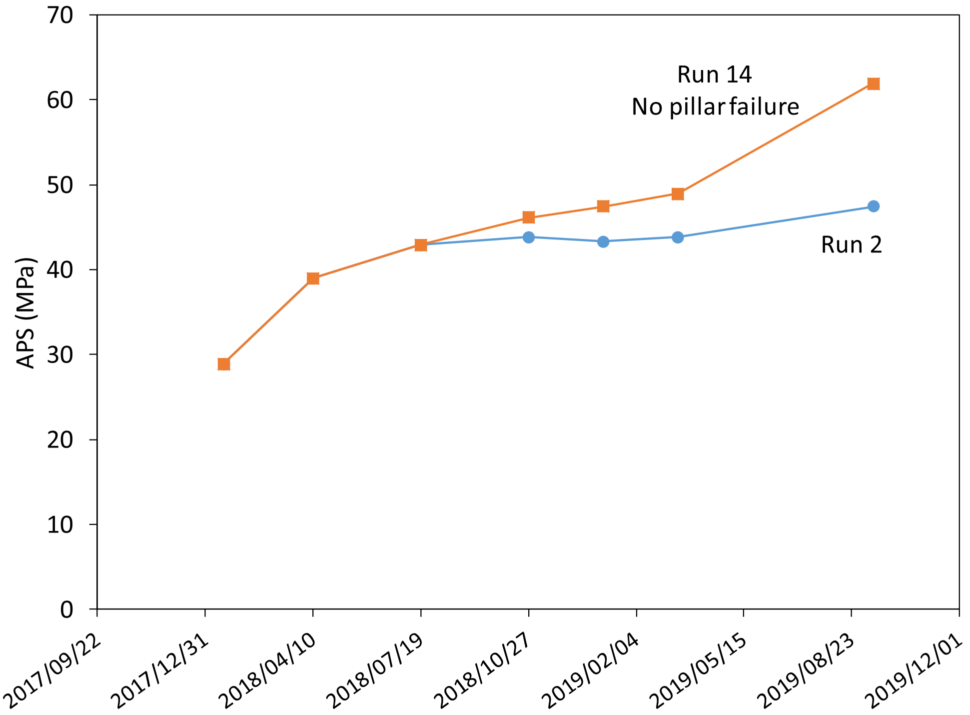

replication of the observed pillar damage trends and stope closure values as pillar extraction or pillar formation proceeds. The use of an unstructured triangular element mesh enables the simulation of irregular pillar shapes and mining steps. The study does illustrate the difficulty in obtaining exact replications of actual pillar deformation modes. In particular, further development of an enhanced model for the edge spalling zone is warranted.

7 Conclusions

A fast marching method is described to solve the confining seam-parallel stress in a simplified model of the fracture zone in narrow seam or reef deposits with particular emphasis on the solution of pillar mining problems. The method is implemented specifically in a displacement discontinuity boundary element context that is amenable to the solution of large-scale tabular layout problems. The fast marching algorithm is implemented using a triangular element solution mesh that covers both the centers and vertices of the triangular boundary element mesh. The boundary element mesh itself provides a flexible description of irregular plan-view pillar shapes and mining sequences.

The excavation edge failure zone is modelled using a limit equilibrium representation of the seam-parallel and seam-normal stress values. The behavior of this model is examined analytically for the special cases of a uniformly compressed strip pillar and square pillar. The analytic stress–strain response is demonstrated to depend on three non-dimensional parameters Q, M and β. Parameter Q represents the ratio of the limit failed uniaxial strength to the intact material strength and M is the ratio of the failed limit strength envelope slope to the intact strength envelope slope. Parameter β is proportional to the pillar width to height ratio. Pillar size scale effects are not considered. The analysis allows both pillar softening and hardening responses to be represented depending on the choice of the parameters Q, M and β. The analytic model is used as well to verify the numerical values that are calculated using the fast marching algorithm for the case of a uniformly compressed square pillar.

Results from a field study of pillar extraction in a shallow platinum mine are presented and have been used to gauge the viability of the proposed model. It is demonstrated that the model can provide a satisfactory qualitative replication of the observed pillar damage evolution and observed trends in the seam closure as the pillar extraction mining steps were carried out. It is noted as well that some effort is required to guide the correct choice of model parameters.

Future work is planned to enhance the current model to include a transition zone region near excavation edges which can improve the representation of brittle edge spalling effects. This addition should facilitate the simulation of hard rock time-dependent crush pillar or coal pillar scaling effects. Additional investigations of multiple mining horizon problems and stiff reef-parallel layer representations will be pursued.

References

Barron K (1984) An analytical approach to the design of coal pillars. CIM Bull 77:37–44

Barron K, Pen Y (1992) A revised model for coal pillars. In: proceedings of the workshop on coal pillar mechanics and design. Pittsburgh, PA: US department of the interior, bureau of mines, IC 9315: 144–157

Bieniawski ZT, Van Heerden WL (1975) The significance of in situ tests on large rock specimens. Int J Rock Mech Min Sci Geomech Abstr 12:101–113

Crouch SL, Starfield AM (1983) Boundary element methods in solid mechanics. George Allen and Unwin, London

Deist FH, Georgiadis E, Moris JPE (1972) Computer applications in rock mechanics. J S Afr Inst Min Metall 72:265–272

Du Plessis M, Malan DF (2015) Crush pillar support: designing for controlled pillar failure. J S Afr Inst Min Metall 115:481–488

Esterhuizen GS, Dolinar DR, Ellenberger JL (2011) Pillar strength in underground stone mines in the United States. Int J Rock Mech Min Sci 48:42–50

Esterhuizen GS, Tyrna PL, Murphy MM (2019) A case study of the collapse of slender pillars affected by through-going discontinuities at a limestone mine in Pennsylvania. Rock Mech Rock Engng 52:4941–4952

Garza-Cruz T, Pierce M, Board M (2019) Effect of shear stresses on pillar stability: a back analysis of the Troy Mine experience to predict pillar performance at Montanore Mine. Rock Mech Rock Engng 52:4979–4996

Gonzalez-Nicieza C, Alvarez-Fernandez M, Menendez-Diaz A (2006) A comparative analysis of pillar design methods and its application to marble mines. Rock Mech Rock Engng 39:421–444

Heasley KA (1998) Numerical modeling of coal mines with a laminated displacement-discontinuity code. PhD dissertation, Colorado school of mines

Hedley DGF, Grant F (1972) Stope-and-pillar design for Elliot Lake uranium mines. Bull Can Instit Min Metall 65:37–44

Kimmel R, Sethian JA (1998) Computing geodesic paths on manifolds. Proc Natl Acad Sci USA 95:8431–8435

Lunder PJ, Pakalnis R (1997) Determination of the strength of hard rock mine pillars. Bull Can Instit Min Metall 68:55–67

Malan DF, Napier JAL (2011) The design of stable pillars in the Bushveld mines: a problem solved? J S Afr Inst Min Metall 111:821–836

Malan DF, Napier JAL (2018) Reassessing continuous stope closure data using a limit equilibrium displacement discontinuity model. J S Afr Inst Min Metall 118:227–234

Martin CD, Maybee WG (2000) The strength of hard-rock pillars. Int J Rock Mech Min Sci 37:1239–1246

Napier JAL (2016) Application of a fast marching method to model the development of the fracture zone at the edges of tabular mine excavations. 50th US rock mechanics/geomechanics symposium, Houston, Texas, USA

Napier JAL, Malan DF (2007) The computational analysis of shallow depth tabular mining problems. J S Afr Inst Min Metall 107:725–742

Napier JAL, Malan DF (2011) Numerical computation of average pillar stress and implications for pillar design. J S Afr Inst Min Metall 111:837–846

Napier JAL, Malan DF (2018) Simulation of tabular mine face advance rates using a simplified fracture zone model. Int J Rock Mech Min Sci 109:105–114

Osher S, Sethian JA (1988) Fronts propagating with curvature-dependent speed. Algorithms based on Hamilton-Jacobi formulations. J Comput Phys 79:12–49

Plewman RP, Deist FH, Ortlepp WD (1969) The development and application of a digital computer method for the solution of strata control problems. J S Afr Inst Min Metall 70:33–44

Ryder JA, Jager AJ (2002) A textbook on rock mechanics for tabular hard rock mines. Safety in Mines Research Advisory Committee, Johannesburg

Ryder JA, Napier JAL (1985) Error analysis and design of a large-scale tabular mining stress analyser. 5th international conference on numerical methods in geomechanics, 1549–1555, Nagoya, Japan

Salamon MDG (1964) Elastic analysis of displacements and stresses induced by mining of seam or reef deposits: II. Practical methods of determining displacements, strain and stress components from a given mining geometry. J S Afr Inst Min Metall 64:197–218

Salamon MDG (1992) Strength and stability of coal pillars. In: proceedings of the workshop on coal pillar mechanics and design. Pittsburgh, PA: US department of the interior, bureau of mines, IC 9315; 94–121

Sethian JA (1999) Level set methods and fast marching methods - Evolving interfaces in computational geometry, fluid mechanics, computer vision, and material science. In: Part of cambridge monographs on applied and computational mathematics, 2nd edn. ISBN 9780521645577

Van der Merwe JN, Madden BJ (2010) Second edition of rock engineering for underground coal mining. The Southern African Institute of Mining and Metallurgy, Republic of South Africa. ISBN 978-1-920410-06-3

Wagner H (1974) Pillar design in coal mines. J S Afr Inst Min Metall 80:37–45

Watson BP, Ryder JA, Kataka MO, Kuijpers JS, Leteane FP (2008) Merensky pillar strength formulae based on back analysis of pillar failures at Impala Platinum. J S Afr Inst Min Metall 108:449–461

Wilson AH (1972) A hypothesis concerning pillar stability. Min Eng 131:409–417